Chapter 3

Grazing-Incidence Small Angle X-Ray Scattering in Polymer Thin Films Utilizing Low-Energy X-Rays

Katsuhiro Yamamoto

Additional information is available at the end of the chapter

http://dx.doi.org/10.5772/65090

Abstract

The intricate nanoscopic morphology of soft materials such as block copolymer and polymer blend system successfully analyzed by small angle X-ray scatterings (SAXS). In thin films, those soft material systems have attracted great attention because of a potential for practical use of functional materials. The morphology has been revealed by grazing-incidence (GI) methods. Recently, advanced grazing-incidence technique for analysis for surface-, volume-, and material-sensitive method (high time, spatial, and/or material resolution) has been reported. Using low X-ray photon energy, tender X-ray (1–4 eV) and soft X-ray near *K*-edge carbon, allows probing a complex nanomorphology with those sensitivity. In this chapter, recent GI-SAXS with tender X-ray and resonant soft X-ray (GI-RSoX) will be picked up to open for discussion on new possibility of structural analyses.

Keywords: grazing-incidence X-ray scattering, organic thin film, block copolymer, tender X-rays, depth profiling

1. Introduction

Block copolymer (BCP) composed of two (more) immiscible polymers form variety structures with the periodicity of several tens nanometer both in bulk and thin films. BCP thin film has attracted great attention as an applicable material to various fields, e.g., solar cell [1–3], nanolithography [4–6], and size-selective separation [7, 8]. In bulk state, microphase-separated structure is predicted by the Flory-Huggins interaction parameter, the degree of polymerization, and the volume fraction of blocks [9], whereas in thin film, film thickness [10, 11] and substrate-polymer interaction and/or also polymer-air interaction[12] must be taken into

consideration. Controlling morphology, orientation and size of the structures are necessary for practical use although phase-separation behavior of BCP in thin film becomes more complicated. This has motivated numerous orientation control methodology studies that have examined the influence of film thickness [10, 11, 13, 14], surface/or interfacial free energy [14–17], surface topology [15, 18, 19], external applied fields (shear-induced [4, 20], electric field [21], magnetic field [22], and light-driven [23, 24]), solvent vapor or thermal annealing[25–30], and directional solidification [31–33]. Since functionality and physical property are also strongly related to the structure and the mobility in the vicinity of interface, revealing structure in detail is required. Suitable characterization techniques are required to monitor the structures of BCP both laterally and in-depth. Several approaches have been used to find BCP structures. Atomic force microscopy (AFM), electron microscopy, dynamic secondary ion mass spectrometry (DSIMS), X-ray photoelectron spectroscopy (XPS), grazing incidence small angle X-ray or neutron scattering (GISAXS, GISANS), X-ray or neutron reflectivity (XRR, NR), etc. have been used to study the structure of BCP thin films. AFM can enable an access of the information only near the surface although the surface structure can be directly observed and easily understandable. Electron microscopy is a powerful tool for visually examining a cross-sectional view of polymeric thin films in two-and three-dimensional real space [34]. DSIMS can elucidate the BCP morphology and the self-diffusion of polymer chains in thin films along a depth direction [35]. Time-of-flight (ToF) SIMS using ion cluster beam was reported to be a particularly well-suited technique that enables the in-depth profiling of polymers [36, 37]. X-ray photoelectron spectroscopy depth profiling with $C60^{+}$ sputtering revealed the ion distribution in lithium salt-doped BCP thin films [38, 39].Electron microscopy, DSIMS, and XPS techniques are essentially accompanied by the destruction of specimen because of processing such as sectioning or etching for analysis. In particular, it is important to take into account the deformation and losing of a precise original spatial coordinate induced by sectioning and chemical reactions induced by etching in the analysis of results obtained by these techniques. In contrast, neutron reflectivity (NRR) measurements enable a practically nondestructive analysis of depth profiles and ordering of microphase-separated structure in BCP thin films [40, 41]. However, the NRR provides structural information (density profile) only in the vertical direction to the sample surface and lateral information of the structure is inaccessible. In addition, accuracy of the density profile (depth-resolved information) perpendicular to the surface becomes worse when the film thickness is large for analyzing periodicity of microphase-separated structure. Generally, NRR depth profiling is suited for very thin film (less than 100 nm) as in the above case. GISAXS is another very powerful tool for understanding the nanostructure in both vertical and lateral directions of organic thin film (BCP thin film). And GISAXS is essentially nondestructive method under the condition of the no radiation damage of X-rays [42–47]. Commonly, SAXS and GISAXS methods have been conducted using hard X-rays with energy range of 6–14 keV. However, under these conditions, the penetration depth of X-rays rapidly reaches the thickness scale of the organic materials in the vicinity of the critical angle α_C of total reflection at the polymeric surface, which is making depth-resolved GISAXS measurements with hard X-rays totally impractical. A depth-sensitive GISAXS method using tender X-ray (1.77 keV) was first reported for the BCP thin film by Okuda et al. [48] and Wernecke et al. [49]. They investigated the structural relaxation near the

http://dx.doi.org/10.5772/65090

surface and the dynamic heterogeneity of polymer chains in thin films. At even lower X-ray photon energies, near the adsorption *K* edges of the polymeric materials (the oxygen, nitrogen, and carbon *K* edges), the fine structure of the adsorption edge can be utilized in GISAXS as reported by Ruderer et al. [50]. The grazing-incidence resonant soft X-ray (GI-RSoXS) has been applied for polymer blend thin films with low contrast in the real part of the refractive index for the hard X-rays but with significant differences in the soft X-ray regime. Furthermore, the X-ray penetration depth is drastically affected by the changes in the X-ray photon energy across the *K*-edge. The surface-and volume-sensitive structure of polymer blend films had been analyzed using this technique [50]. Similar to the GISAXS, GISANS has been developed by Müller-Buschbaum and co-workers. GISANS is a perfectly nondestructive approach for structure analysis and has essentially the same capability for surface-sensitive [51], interface-sensitive (structural information near the polymer-substrate interface enabled by the ability of the neutrons to go through the substrate) [52, 53], and depth-sensitive analysis [54]. Moreover, in time-of-flight mode GISANS (ToF-GISANS) [52, 55] a broad wavelength band is used instead of a single neutron wavelength, i.e., a range of different scattering vectors is directly probed by the measurement under a fixed angle of incidence. At an appropriate incident angle, it is possible to simultaneously conduct surface- and bulk-sensitive measurements. While GISANS possesses advantages as compared with the GISAXS, GISANS experiments still remain very rare because GISANS requires very high-flux sources to measure the much weaker signals in grazing-incidence geometry and the need for deuterium labeling (in some cases, of course, this is beneficial for structure analysis by tuning the contrast). These GISANS techniques have been well summarized in the reviews [56].

In this chapter, recent advanced GISAXS experiment utilizing low-energy X-rays will be introduced. GISAXS probes the complex nano- and microphase-separated structure in polymer thin films. Especially, tuning the energy of GISAXS in the tender and soft X-ray regime allows to the tailoring of X-ray penetration depth and contrast and thereby the probing of more complex morphologies in polymer thin films. GI-RSoXS has been applied for polymer blend thin films with low contrast in the real part of the refractive index for the hard X-rays but with significant differences in the soft X-ray regime. Furthermore, the X-ray penetration depth is drastically affected by the changes in the X-ray photon energy across the *K*-edge. The surface-and volume-sensitive structure of polymer blend films had been analyzed using this technique.

2. Grazing-incidence small angle X-ray scattering

Incident X-ray beam goes into the sample surface at a very shallow angle α_i (normally less than 1°). Scattering is measured with a two-dimensional detector as a function of the exit angle α_f (out-of-plane angle) and the in-plane angle 2Θ. The magnitude of the scattering vector is given by $q = 4\pi\sin\theta/\lambda$($\lambda$: wavelength of X-ray, 2θ: scattering angle). The scattering vector q_z means the component vertical to the film surface. The q_x and q_y are the components of scattering vectors in the sample surface, perpendicular to and directed to the X-ray beam, respectively. For each data set *I*(y, z), pixels of the detector were converted into exit angle α_f normal to the

sample surface and a scattering angle 2Θ parallel to the surface by simple geometrical consideration. The amplitude of scattering vector q is composed of q_x, q_y, and q_z related to the experimental angles by

$$q = \begin{pmatrix} q_x \\ q_y \\ q_z \end{pmatrix} = \frac{2\pi}{\lambda} \begin{pmatrix} \cos 2\Theta \cos\alpha_f - \cos\alpha_i \\ \sin 2\Theta \cos\alpha_f \\ \sin\alpha_i + \sin\alpha_f \end{pmatrix}, \quad (1)$$

As shown in **Figure 1**, typical sample-to-detector distances (SSD) for GISAXS are of the order of 1–2 m. In the case of small angle scattering, the two-dimensional detector probes mainly the q_y and q_z information because q_x is very small and the curvature of the Ewald sphere is negligible. The calculation of the out-of-plane scattering vector is considerably complex. Above critical angle α_C of polymeric materials, the theoretical penetration depth is much larger than the film thickness (order of micro-meter) (when hard X-ray is normally used) as shown in **Figure 2**. The transmitted wave can therefore be reflected at the polymer-substrate interface in combination with diffraction from the structures in the thin film. Under the assumption that each X-ray scatters no more than once from the objects and there is no transmission through the substrate, there are four possible scattering events to happen, additionally refraction at the sample surface (air-polymer interface) (**Figure 3**).

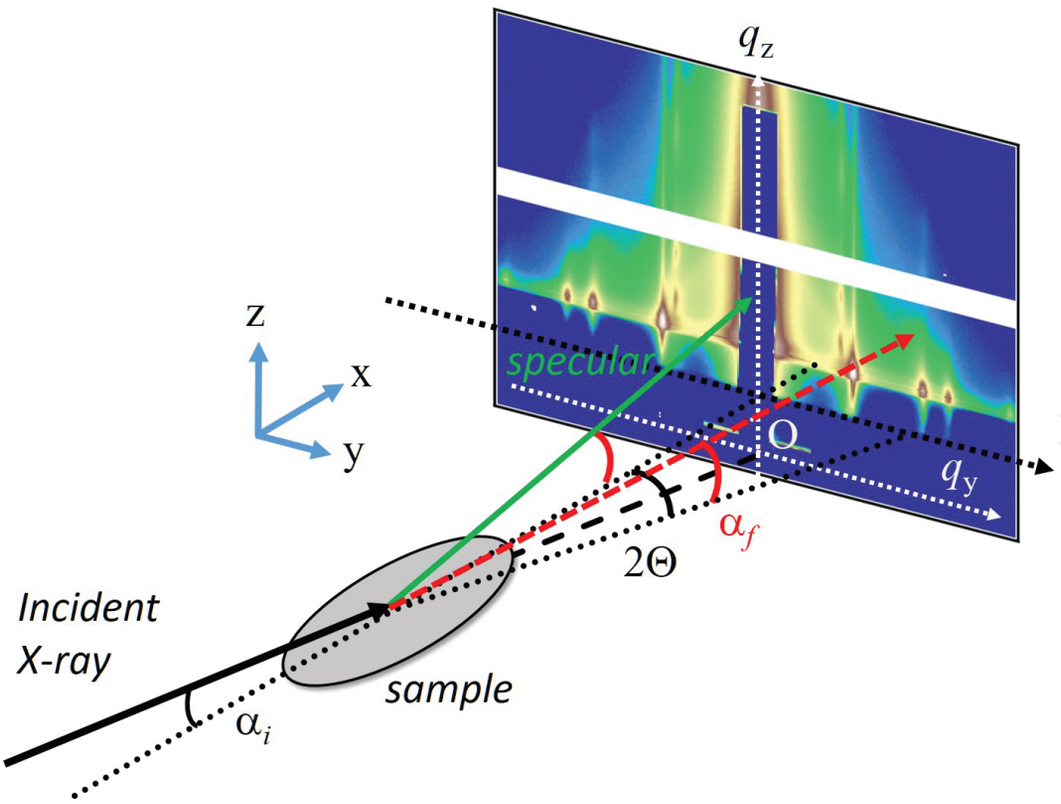

Figure 1. Schematic illustration of the scattering geometry used in GISAXS. The sample surface is inclined by incident angle with respect to the horizon. The exit and in-plane angles are denoted α_i and 2Θ, reepectively.

http://dx.doi.org/10.5772/65090

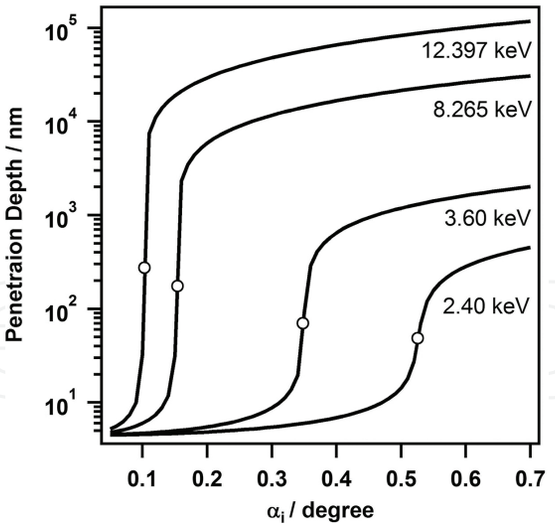

Figure 2. Penetration depth calculated for a block copolymer (S2VP) film for different X-ray energies, 12.397, 8.265, 3.60, and 2.40 keV.

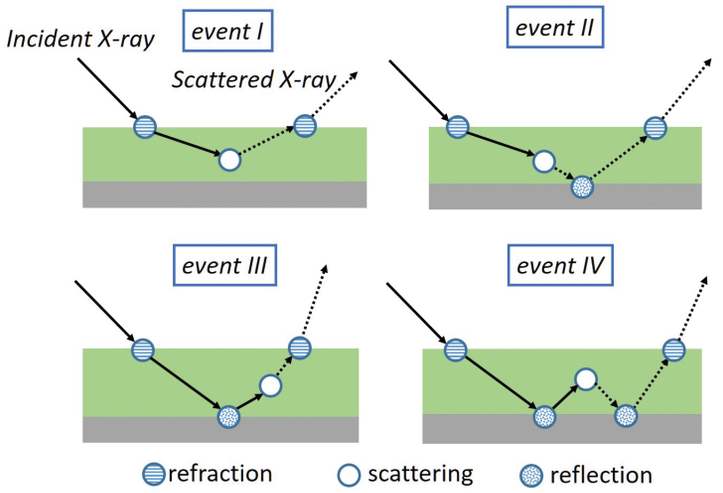

Figure 3. Four scattering events, demonstrating different combinations of reflection from the substrate with diffraction from the objects.

3. Depth-resolved structure analysis of microphase-separated structures in block copolymer thin film by grazing-incidence small angle X-ray scattering utilizing tender X-ray

3.1. Cylindrical microdomain in block copolymer thin film [57]

In this section, GISAXS measurement with low energy (tender) X-ray (2.40 keV) is introduced in order to precisely elucidate the depth profile of a microphase-separated structure (hexago-

nally packed cylinders) of a polystyrene-b-poly (2-vinylpyridine (S2VP) thin film on a silicon wafer with the cylindrical microdomains (poly (2-vinylpyridine): P2VP) oriented parallel to the substrate after the appropriate thermal annealing in vacuum. The cylindrical domains in the S2VP thin film were preferentially oriented parallel to the surface of the substrate induced by the surface free energies and/or an interfacial interaction between S2VP and the substrate. In GISAXS, the structural parameters of the cylindrical domains in both the lateral and vertical directions are accessible because the diffraction spots appear with the offset in the q_y direction.

S2VP thin film (number average molecular weight M_n = 26,400, molecular weight polydispersity index = 1.24, and φ_{PS} = 76.3 vol%) was prepared by spin casting from toluene solution (10 wt%) of S2VP onto a silicon wafer substrate at 3000 rpm for 30 s. Subsequently, the S2VP thin film was thermally annealed under vacuum at 170 °C for 48 h. The sample surface was composed of PS component (X-ray photoelectron spectroscopy and water contact angle [58], predicted by surface free energies of components [59]) was a very flat and smooth examined by atomic force microscopy and optical white-light interferometer microscopy measurements.

Tender X-ray GISAXS measurement (room temperature) was performed at BL15A2 [60] at the Photon Factory, KEK, Tsukuba in Japan. The BL15A2 is an undulator beamline where X-rays in a wide energy range from 2.1 to 15 keV (energy resolution is 2×10^{-4}) is available. In this study, the energy of X-ray was set at 2.40 keV (the wavelength of 5.16 Å) and the sample-to-detector distance (SDD) was 830 ± 5 mm. The accuracy of the camera lengths arises from the scattering vector calibration on a detector with a standard specimen and a footprint of the incident beam on the sample surface (sample size of c.a.1 cm). The X-ray incident angle was varied between 0.290° and 0.620° and PILATUS 2M designed for usage in vacuum was used as a detector for the 2D scattering pattern. X-ray exposure time of 300 s was sufficient to obtain a clear scattering pattern. Hard X-ray (wavelength 1.0 Å) GISAXS measurements were performed at BL10C in Photon Factory and BL03XU57 in SPring-8, Harima, Japan using PILATUS 2M and CCD (Hamamatsu Photonics) detectors with SDD of 2.3 m. All detectors were calibrated using lead stearate prepared in-house (d = 5.01 nm, calibrated).

The X-ray penetration depth Λ is defined as the depth at which the X-ray intensity is attenuated by 1/e. The value of Λ depends on X-ray energy (wavelength λ), the critical angle, α_C, of total reflection, and the incident angle α_i. Surface roughness influences practically the penetration depth of X-rays because various α_i are provided. The roughness of the surface used here is regarded as sufficiently small to estimate the penetration depth as evidenced by the clear observation of the critical angle in XRR. Under experimental conditions with the ideally flat surface, Λ is given by

$$\Lambda = \frac{\lambda}{4\pi}\sqrt{\frac{2}{\sqrt{(\alpha_i^2 - \alpha_c^2)^2 + 4\beta^2} - (\alpha_i^2 - \alpha_c^2)}}, \tag{2}$$

http://dx.doi.org/10.5772/65090

where β is the imaginary part of the complex refractive index. The critical angle α_C is specified as $\alpha_c \sim \sqrt{2\delta}$ where δ is deviation from the real part of the refractive index, δ and β are given by

$$\delta = \left(r_e \lambda^2 N_A / 2\pi\right) \rho_M \sum_Z w_Z \left(f_{0Z} + f'_Z(E)\right) / \sum_Z w_i A_Z, \tag{3}$$

$$\beta = \left(r_e \lambda^2 N_A / 2\pi\right) \rho_M \sum_Z w_Z f''_Z(E) / \sum_Z w_Z A_Z, \tag{4}$$

where r_e is the classical electron radius (2.82×10^{-5} Å), N_A is Avogadro's number, ρ_M is the mass density, w_Z is the fraction of element Z, $A_{Z,}$ is the relative atomic mass, f_{0Z} is the nonresonant term of the atomic scattering factor corresponding to the atomic number, and $f'_Z(E)$ and $f''_Z(E)$ are the real and imaginary parts of the anomalous dispersion for the incident X-ray energy E, respectively. For example, here we used 4.1468×10^{-5} for δ and 7.0239×10^{-7} for β of PS at 2.40 keV. The α_c value of S2VP thin film using GISAXS and XRR measurements was obtained. The calculated S2VP penetration depth is shown in **Figure 2**. It is hard to precisely control the penetration depth Λ at the nanometer scale for GISAXS experiment conducted using hard X-rays (8–12.4 keV) because the value of Λ rises steeply at α_C. On the other hand, as the X-ray energy decreases, Λ changes more gradually near the critical angle and shows decreased depth values at angles even greater than α_C. Hence, better control ofΛ is expected for depth-resolved GISAXS measurements using tender X-ray (2.40 keV) because of the critical angle and attenuation coefficient values that are much greater than those for the hard X-rays.

GISAXS measurements of the S2VP thin film (thickness of 420 nm) using tender X-ray were performed at various incident angles and many Bragg spots were measured as shown for large α_i in **Figure 4**. All spots were assigned to parallel oriented hexagonally packed cylinders. GISAXS patterns at approximately q_y of 0.26 nm^{-1} are presented in **Figure 4(c)** and **(d)** and show a remarkable elongation of the Bragg spots in the q_z direction for smaller α_i. One-dimensional scattering profiles vertically cut at q_y = 0.26 nm^{-1} with various incident angles are shown in **Figure 5**. Bragg peaks were assigned to the scattering from transmitted (denoted by T) and reflected (denoted by R) beams by the substrate. These two scattering events are typically noticeable in GISAXS measurements [45, 46]. The second-order peaks derived from (11) reflection at q_z approximately 0.6 and 0.7 nm^{-1} were used for structure analysis because the primary peak from the (10) plans was partially invisible due to the detector gap. The magnitudes of the Bragg spot full widths at half maximum (FWHM) varied in the vicinity of the α_C, with larger FWHM values observed at smaller incident angles.

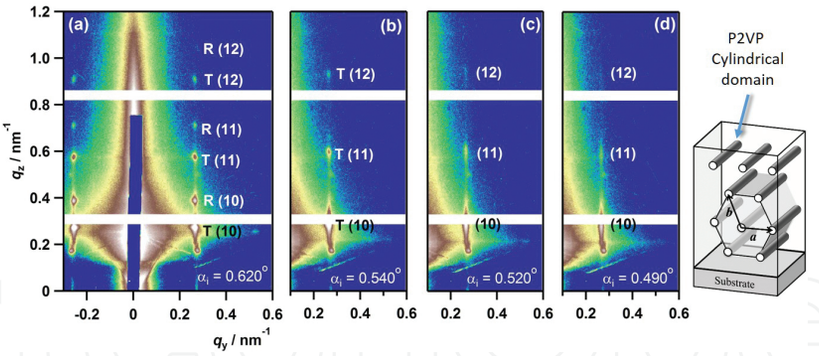

Figure 4. 2D-GISAXS (with λ of 5.166Å) patterns of S2VP-25k thin film annealed for 48 h at 170°C. (a) α_i was set at 0.62° ($\alpha_i > \alpha_C$), (b) 0.54°($\alpha_i > \alpha_C$), (c) 0.52°($\alpha_i < \alpha_C$), and (d) 0.49° ($\alpha_i > \alpha_C$). Schematic illustration represents the cross section of cylindrical microdomains in the thin film forming HEX aligned parallel to the substrate.

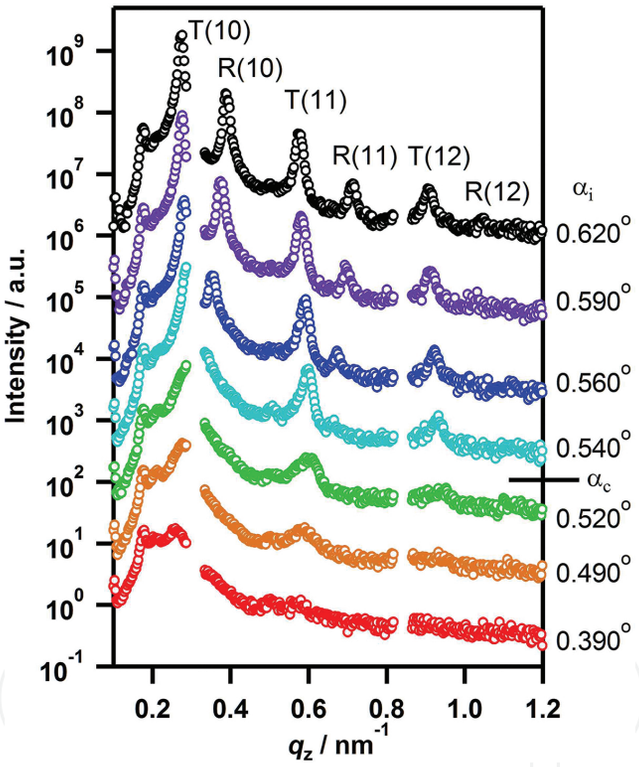

Figure 5. One-dimensional GISAXS profiles along q_z direction obtained by vertical cut at q_y = 0.26 mn^{-1}. Reprinted with permission from Saito et al. [57]. Copyright 2015 American Chemical Society.

The observed peak broadening can be interpreted by the change in the penetration depth. While generally such broadening can be understood by either the grain size effect and/or disordering of the crystal lattice, the FWHM in the q_y indicated no change irrespective of the incident angles as shown in **Figure 6**, eliminating the influence of the lattice disordering because the broadening was mainly seen in the q_z direction and the size effect was dominantly considered. Rather, the broadening in this case is because of the reduction in the size of the

http://dx.doi.org/10.5772/65090

observed region. The FWHM of a scattering peak depends on the grain size of a crystal, as expressed by the Laue function, $L(q)$

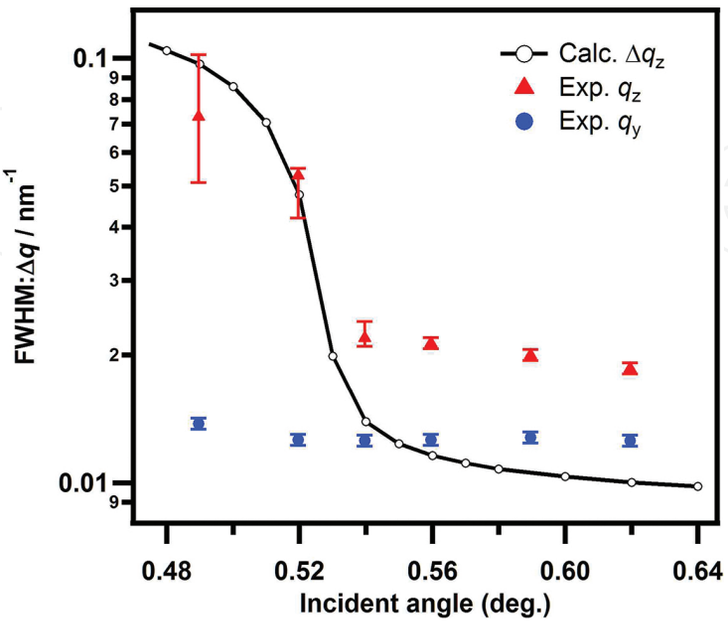

Figure 6. FWHM values of (11) Bragg spots obtained experimentally and calculated using Eq. (6). Reprinted with permission from Saito et al. [57]. Copyright 2015 American Chemical Society.

$$L(\boldsymbol{q}_z) = \sum_N \exp(iN\boldsymbol{q}_Z \cdot \boldsymbol{b}) = \frac{\sin\left[(N+1)\boldsymbol{q}_z \cdot \boldsymbol{b}/2\right]}{\sin\left[\boldsymbol{q}_z \cdot \boldsymbol{b}/2\right]}, \tag{5}$$

where N is the number of the reflection plane and $\boldsymbol{b}$ is the unit lattice vector related to z-direction normal to the surface. Here, the X-ray wave decays exponentially, and considering attenuation decay, the Laue function can be re-expressed as

$$L(\boldsymbol{q}_z) = \sum_N \frac{\sin[(N+1)q_z \cdot D_{01}/2]}{\sin[q_z \cdot D_{01}/2]} \exp\left[-\frac{\left(\frac{1}{2}+\frac{2}{3}N\right)D_{01}}{2\Lambda}\right], \tag{6}$$

where D_{01} is the periodicity of the (01) plane. Since the scattering intensity is proportional to the square of the Laue function, the FWHM can be calculated simply. The FWHM of the Bragg spots of the T (11) plane in q_z direction experimentally obtained is shown in **Figure 6**. The calculated values for FWHM in the q_z direction for the penetration depth Λ given by Eq. (2)

are also plotted in **Figure 6**. The change in the calculated width shows the same trend as the experimental results, indicating that the broadening of the Bragg spots can be explained by the size effect determined by the depth Λ. Thus, the observed region of GISAXS measurement can be controlled with the incident angle, enabling depth-resolved GISAXS.

When $\alpha_i < \alpha_C$, X-rays travel on the surface of the film and cannot propagate in the film. Only the evanescent wave can penetrate from the sample surface into the film. In this situation, the scattering peak α_z along the q_z direction is observed at the position given by the sum of the incident angle and the true scattering angle α_S derived from the period of the observed structure. Thus, α_s can be given as follows:

$$\alpha_S = \alpha_Z - \alpha_i \tag{7}$$

Using above relation, the true q_z value of the (11) spot can be estimated from the experimental peaks. On the other hand, in the case of $\alpha_i < \alpha_C$, an X-ray wave can travel into the film. The X-ray first refracts at the sample surface, goes through the film, is reflected by the interface between the sample and substrate, and finally exits out of the film surface with refraction as shown in **Figure 3**. Normally, some scattering events in GISAXS experiments occur because of the refracted X-rays at the polymer surface and reflected X-ray on the substrate surface, resulted in appearance of a number of scattering peaks. The scattering cross-section for GISAXS of the block copolymer thin film has been calculated within the framework of the distorted wave Born approximation (DWBA) [61]. Lee et al. [44], Yoon et al. [44, 45], and Busch et al. [46, 47] introduced the DWBA (or a combination of Bragg's and Snell's laws, refraction and reflection) to estimate the scattering peak positions. Scattering intensity due to the incident X-ray (transmission) and reflected X-ray (reflection) were pronounced. Debye-Scherrer rings of the block copolymer films with powder-like orientation of lamellar domains. The scattering peaks arising from transmitted and reflected X-rays at the substrate can be calculated following [53]

$$q_z = \frac{2\pi}{\lambda}\left[\sin\alpha_i + \left\{\sin^2\alpha_c + \left[\left\{\left(\frac{m\lambda}{D}\right)^2 - \left(\frac{q_y\lambda}{2\pi}\right)^2\right\}^{\frac{1}{2}} \mp (\sin^2\alpha_i - \sin^2\alpha_c)^{\frac{1}{2}}\right]^2\right\}^{\frac{1}{2}}\right], \tag{8}$$

where m represents the peak order, which is $3^{1/2}$ for the (11) plane in hexagonally packed cylindrical microdomains. The upper (−) and lower (+) branches in the equation indicate the Bragg diffraction of the transmitted and reflected X-rays, respectively. D is the characteristic length of the given plane. As for the (11) plane, Eq. (9) can be derived from Eq. (8) as follows:

$$q_z = \frac{2\pi}{\lambda}\left[\sin\alpha_i + \left\{\sin^2\alpha_c + \left[\frac{3\lambda}{2D} \mp (\sin^2\alpha_i - \sin^2\alpha_c)^{\frac{1}{2}}\right]^2\right\}^{\frac{1}{2}}\right], \tag{9}$$

http://dx.doi.org/10.5772/65090

where D corresponds to the D_{01} in this case. When the D_{01} was set to 18.8 nm, the DWBA calculation Eqs. (8) and (9) gave the best representation for all Bragg spots as shown by crosses in **Figure 7**.

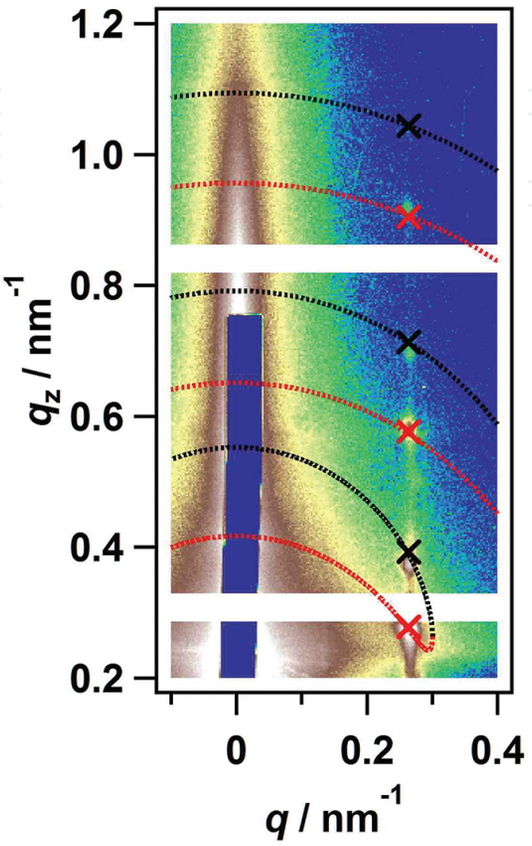

Figure 7. GISAXS patterns measured with tender X-ray (2.40 keV) at the angle of incidence 0.620. The dotted lines of the calculated Debye-Scherrer like rings from transmitted (red) and reflected (black) beams obtained using Eq. (8) as assuming the characteristic length $D_{\perp}$ (perpendicular to the surface) is smaller than the $D_{\parallel}$ (virtual parallel component). The $D_{\perp}$ corresponds to D_{01}. The crosses were obtained using Eqs. (8) and (9).

For GISAXS experiment in the soft X-ray region, the large curvature of the Ewald sphere may give rise to an apparent distortion of the GISAXS pattern when the measurements are conducted with a fixed angle of incidence and using the area 2D plane detector. Yamamoto et al. [62] discussed the effect of the Ewald sphere curvature and performed model calculations using DWBA [61]. At the lower energy of 1.77 keV, while the interparticle interference peaks extended and bent inward at large q_z, (approximately 2.0 nm^{-1}), no bending of the extended peaks was observed using hard X-rays. In the presence of the Ewald sphere curvature, the unmodified equation is no longer valid. In this study, Eq. (9) that had been developed for the hard X-ray regime to explain the experimental GISAXS pattern is confirmed to be valid for this observed q-range with tender X-ray regime 2.40 keV [57].

The lattice constant $\boldsymbol{b}$ associated with the direction perpendicular to the surface was slightly smaller than the lateral lattice constant $\boldsymbol{a}$. The hexagonal lattice was slightly deformed, in

particular, the nanocylinders were packed into distorted hexagonal lattice that was laterally elongated and/or vertically collapsed. The distorted hexagonal lattice in polymeric films has been often observed during the drying of solvents [63]. The lattice constant remained almost constant with respect to the depth. In contrast, the constant b and the angle ϕ between the lattice vectors increased with decreasing depth, i.e., approaching the surface, the lattice deformation was relaxed to a normal hexagonal lattice (**Figure 8**).

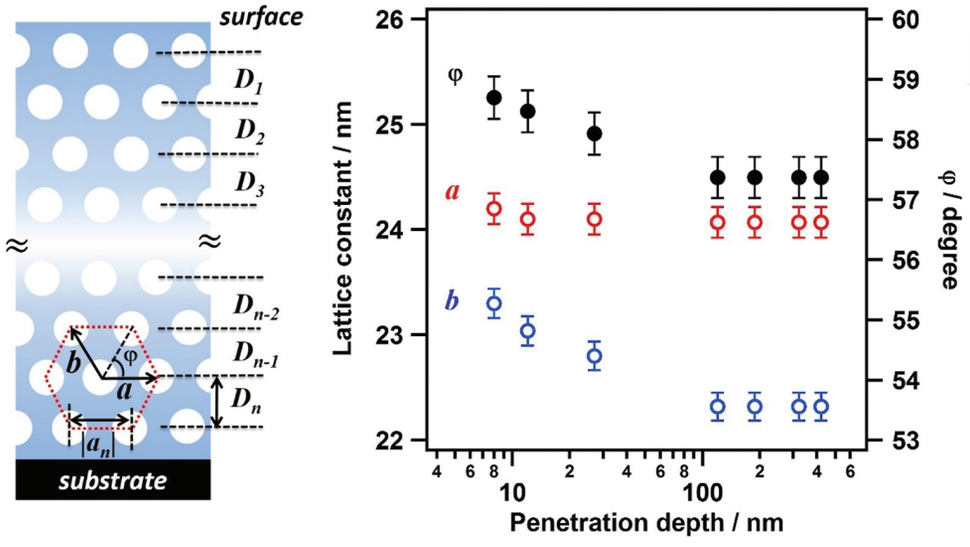

Figure 8. Lattice parameters plotted against the penetration depth (left). Right illustration indicates parallel-aligned cylindrical domains in thin film and the unit cell. The spacing D_n corresponds to the vertical distance neighboring planes (1). $|\boldsymbol{a}_n|$ and $|\boldsymbol{b}_n|$ represents the distance between neighboring cylindrical domains. The following relations were obtained by analysis; $D_1 > D_2 > D_3 > \cdots > D_c = \cdots = D_n$. $|\boldsymbol{a}_0| = |\boldsymbol{a}_1| = \cdots = |\boldsymbol{a}_n|$. $|\boldsymbol{a}_n| > |\boldsymbol{b}_n|$. Here, D_c means D_n reached constant value. Reprinted with permission from Saito et al. [57]. Copyright 2015 American Chemical Society.

3.2. Orientation and relaxation behaviors of lamellar microdomains of poly(methyl methacrylate)-b-poly(n-butyl acrylate) thin film [64]

In this section, we investigated the phase-separation behavior of poly (methyl methacrylate-b-n-butyl acrylate) (PMMA-PnBA) forming a lamellar structure aligned parallel to the substrate after appropriate thermal annealing with GISAXS measurement. The structure development through such as degree of the lamellar orientation and relaxation of the lamellar domain spacing was inquired. Also, the GISAXS with tender X-ray for depth-sensitive analysis was conducted to reveal that the difference of the lamellar domain spacing near the surface from the bulk.

To obtain a thin film of the block copolymer PMMA-b-PnBA (M_n = 32,000, M_w/M_n = 1.17, f_{PMMA} = 0.44), PMMA-b-PnBA in toluene (5 wt% polymer solution) was prepared. The thin film was obtained by spin cast on silicon wafer at 3000 rpm for 30 s. The thin films (thickness was 280±30 nm) were dried at room temperature, subsequently thermal annealing was performed at 160° for given time. GISAXS measurement utilizing hard X-ray and tender (soft) X-ray was performed. Hard X-ray GISAXS measurement was conducted at beamlines BL6A and BL10C

http://dx.doi.org/10.5772/65090

in Photon Factory of KEK, Tsukuba in Japan and BL03XU in SPring-8, Hyogo in Japan [65, 66] with wavelength of 0.15 (BL6A), 0.1488 (BL10C), and 0.1 nm (BL03XU), respectively. Tender X-ray GISAXS measurement was performed at BL15A2 in Photon Factory.

2D GISAXS (hard X-ray) patterns with various annealing times were shown in **Figure 9**. The pattern of as-spun sample (**Figure 9a**) was shaped like an ellipse, which might arise from kinetically frozen or poorly ordered structure. Partially intense scattering was observed at q_z of 0.25–0.28 nm^{-1} where was emphasized due to the so-called Yoneda peak, i.e., it did not indicate specific orientation, suggesting that no orientation of phase-separated structure of PMMA-b-PnBA appeared without thermal annealing. After the sample was thermally annealed for even 1 min, the scattering intensity around $q_y = 0$ (near the beam stop) grew. In addition, two clear ring-shaped scattering patterns like Debye-Scherrer rings were observed. Each scattering ring was arising from transmitted (denoted by T) and reflected (denoted by R) beams as described in previous section. The scattering intensity near beam stop became strong with annealing time. This change in GISAXS pattern indicates the growth of the parallel orientation of the lamellar microdomain. The development of the normalized scattering intensity [64] from parallel lamellar structure is shown in **Figure 10**. Orientation is nearly complete after annealing for 60 min. The GISAXS measurement gave structure information about domain spacing of the lamellar morphology. The domain spacing (D) of the lamellar structures aligned parallel to the surface was estimated. To determine the accurate domain spacing, the distorted wave Born approximation (DWBA) was applied for analysis of the GISAXS patterns. The experimentally estimated D values are also plotted as a function of the annealing time in **Figure 10**. The value of the D approached to the D_0 of the bulk sample (independently obtained to be 21.6 nm) with an increase in annealing time. The D of the parallel orientated structure was slightly smaller than D_0 even after 4 h thermal annealing, i.e., the spacing collapsed vertically. Consequently, the lamellar structure was deformed along the depth direction (similar phenomena as the previous section). Thermal annealing induced the relaxation of the domain spacing and it seems taking approximately more than 2 h to complete the relaxation of D (equals to the value of the bulk)

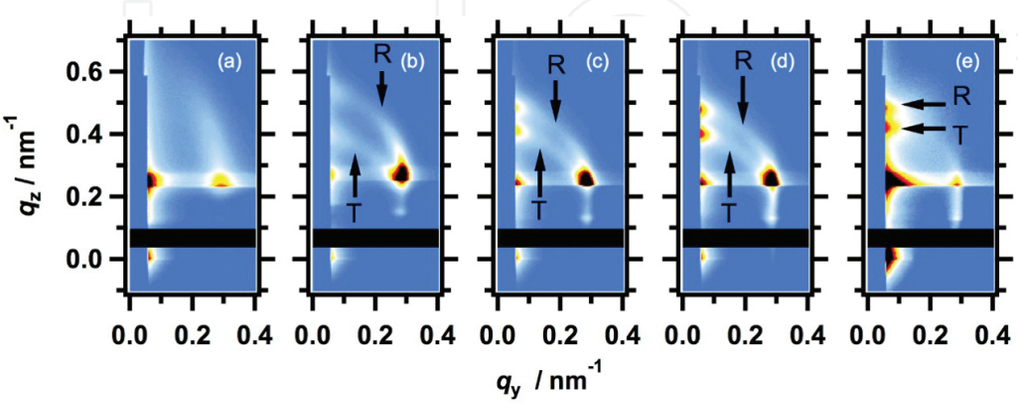

Figure 9. GISAXS patterns (hard X-ray, 1.488 Å) of PMMA-b-PnBA thin film (a) as cast and (b–e) as annealed at 160°C with given annealing time; (b) 1, (c) 3, (d) 5, and (e) 10 min. R and T denoted the scatterings from reflected and transmitted X-rays, respectively. Reprinted from Saito et al. [64]. Copyright Nature Publishing Group.

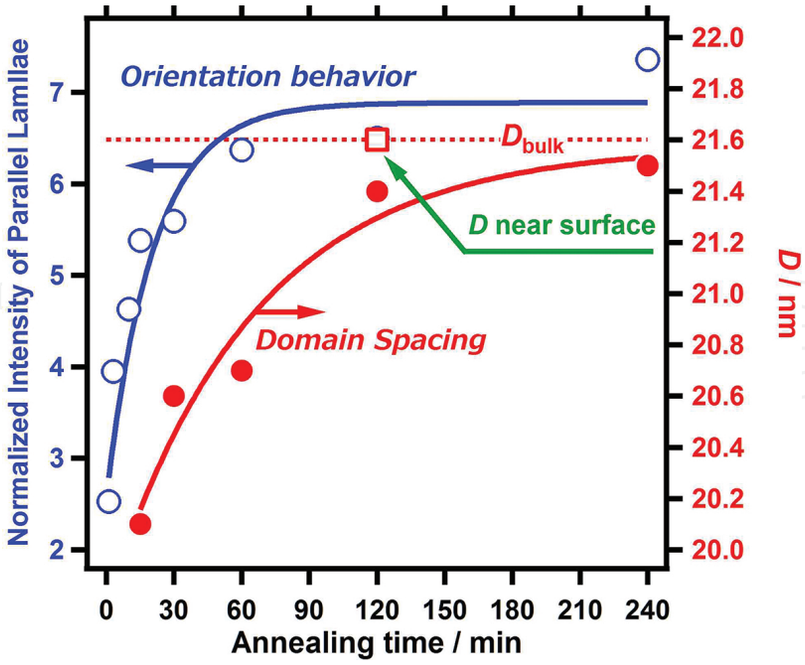

Figure 10. Time evolution of the orientation of the lamellar domain (open circles) and the relaxation of the lamellar *D* (filled circles). The solid lines were drawn as a guide to eyes. Dotted line shows the D_0 value of the bulk. Open square indicates the *D* value near the surface. Reprinted from Saito et al. [64]. Copyright Nature Publishing Group.

As is well known, preferential wetting of surface and substrate interfaces plays an important role of orientation in thin film [12, 17]. In this case, surface energies of PMMA, PnBA, and Si substrate are 41.1, 33.7, and 77.4 ± 0.5 mJ/m^2, respectively [16]. According to the surface free energies, it will be predicted that PMMA segregates to the surface of the silicon substrate, whereas PnBA segregates to air surface. As a result of preferential wetting, the parallel orientation of lamellar structure is induced at the surface and/or the polymer/substrate interfaces and the oriented lamellae propagate into the entire film [67]. In fact, XPS measurement proved that surface molar fractions of PnBA (within a few nanometers) were 80 mol% (repeat unit) in as-cast film and the PnBA component perfectly covered on the surface after thermal annealing with only 60 s. The segregation of each component, orientation of the lamellae, and relaxation of the domain spacing occurred in different time scale. It can be concluded that the PnBA first segregated at air surface within a minute after annealing (PMMA may segregated at the interface), second the microphase-separated structure aligned parallel to the surface, followed by relaxation of the domain spacing.

The polymer thin films have reported to have different mobility dependent on the local region, i.e., near the surface, inside, or near the polymer/substrate interface. It is quite intriguing to investigate that the depth dependence of structure difference exists, in other words, whether there are difference between the structure (orientation, morphology, d-spacing, etc.) in the vicinity of the surface and inside of the film, or not. The GISAXS measurements of PMMA-b-PnBA thin film thermally annealed for 2 h with tender X-ray was performed with various incident angles. As shown in **Figure 11(a)** and **(b)**, in the case of $\alpha_i < \alpha_c$, the scattering (marked arrows) of the lamellar structure oriented parallel to the substrate was considerably diffuse

http://dx.doi.org/10.5772/65090

and broaden, while in the case of $\alpha_i > \alpha_c$, the scattering became clear and sharp. The FWHM values of scattering peak (parallel lamellar domains) in the one-dimensional GISAXS profile obtained vertically cut at various incident angles can be simulated as the same manner of the size effect of measured region as discussed in the previous section (modified the Laue function). Thus, the penetration depth was controlled by changing the incident angle. At near the critical angle, the surface-sensitive measurement is possible as predicted from Eq. (2). The true q_z value of the oriented lamellar structure parallel to the substrate is estimated using the experimentally observed peaks, i.e. D near the surface can be estimated. At α_i of 0.525° (penetration depth Λ of 32.4 nm), D was obtained to be 21.6 nm which is equal to the D_0 value (21.6 nm) of the bulk sample. The value of D near the surface is slightly larger than the value 21.4 nm obtained from DWBA calculation (inside the whole film). This means that relaxation of the domain spacing near the film surface preceded that of the inside. According to previous reports, polymer chain near the surface indicates higher mobility (lower glass transition temperature or viscosity) [68–70]. Moreover, the lamellar structure started to orient from both the air/polymer and polymer/substrate interfaces, which was induced by segregation of one component in the BCP. Therefore, that the faster relaxation of the D of the lamellar structure near the surface was caused by the faster orientation and higher mobility in the vicinity of the surface.

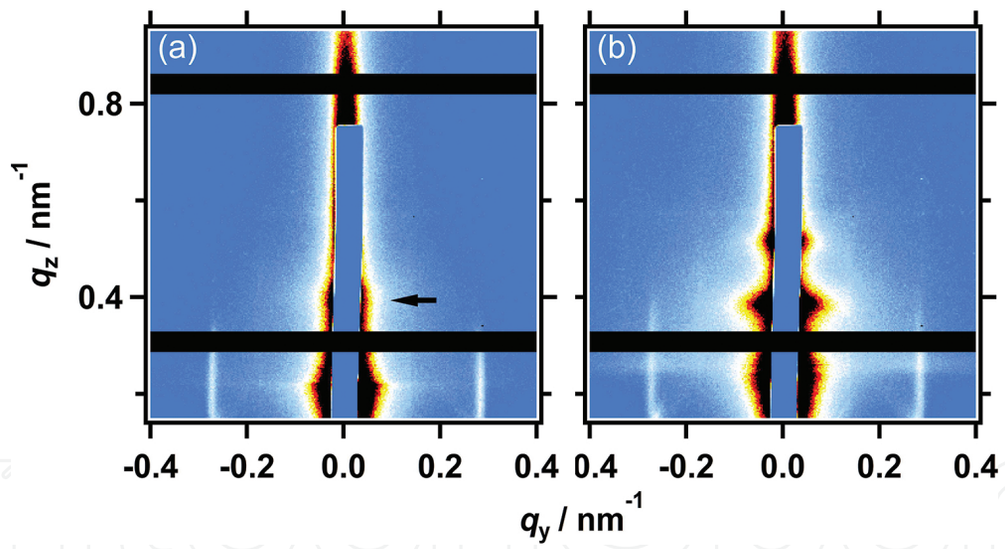

Figure 11. Tender X-ray (2.40 keV) GISAXS patterns of PMMA-b-PnBA thin films annealed at 160 °C for 2 hours at incident angles (a) 0.525° and (b) 0.625°. Reprinted from Saito et al. [64]. Copyright Nature Publishing Group.

3.3. Evaluation of mesogen orientation in thin films of polyacrylate with cyanobiphenyl side chain [71]

Understanding the orientation behavior of polymer chain in the vicinity of interfaces (both substrate and free surfaces) is of practical importance in organic thin film technologies such as coating and photoresisting processes. Thus, a large amount of fundamental knowledge has been ever accumulated. It has been broadly recognized that diverse physical properties of

polymeric materials in ultrathin film state are very different from those in the bulk state. Compared with the vast amount of studies for amorphous and crystalline (LC) polymers, studies on the anomaly in structure and orientation of side chain liquid crystalline polymers in ultrathin film states are rather unexplored. A large number of data related to mesogen orientation have been reported [72–78]. Accordingly, the side chain LC polymers are mostly aligned homeotropically [23, 79–81] The significant effect of the sample surface is apparent from the fact that the mesogen orientation changes to a planer orientation as the sample surface is covered by another layer or material [23, 82–84]. A cyanobiphenyl(CB)-containing polymethacrylate (PCBMA) exceptionally indicated the planar orientation regardless of the fact that the homologous polyacrylate (PCBA) oriented homeotropically [33]. This unexpected orientation behavior is responsible for the difference in the main chain rigidity (but still no rational explanation). In these contexts, the investigation to reveal in detail the orientation of PCBA is proceeded by the GISAXS measurements by systematically changing the film thickness. Additionally, GISAXS with hard (8.05 keV) and tender (2.30 keV) X-rays were carried out.

The side chain LC polymer PCBA (chemical structure shown in **Figure 12**, M_n = 12,000, M_w/M_n = 1.83, glassy state – 13°C (T_g: glass-transition temperature)–smectic A - 95°C (T_i: isotropization temperature)) films on quartz plates were prepared by spin-casting from 0.12–3.0 wt % chloroform solutions to make different thickness samples. The spin-cast film samples were annealed at 135 °C, cooled to a target temperature, kept for 10 min, and then subjected to the measurements. The layer spacing of the smectic A of LC polymers in the bulk was estimated to be 4.6 nm (SAXS). GI-SAXS experiments with hard X-rays (Cu Kα radiation (λ = 0.154 nm)) were conducted with a FR-E X-ray diffractometer equipped with two-dimensional imaging plate R-AXIS IV detector (Rigaku). GI-SAXS experiments using low-energy X-rays were performed at BL-15A2 [60] at the Photon Factory, KEK, Tsukuba, Japan. Experimental details of the GI-SAXS measurements were described in previous sections.

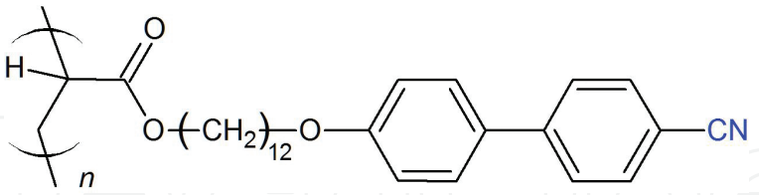

Figure 12. Chemical structure of the side chain LC polymer.

Figure 13 indicates GI-SAXS data measured with hard X-rays (λ = 0.154 nm) for 30 nm thick at 80 °C. For 140 nm thick film, the scattering peaks corresponding to d (smectic layer) = 4.6 nm (100) and 2.3 nm (200) were clearly seen in both out-of-plane and in-plane directions. The intensity of the peaks in the out-of-plane direction was significantly small in 30 nm thick film (as peaks was weakly shown in 1D profile), and no peaks were essentially recognized for 15 nm thick film, although those in the in-plane direction were clearly seen. These results evidently indicate the coexistent of planarly and homeotropically oriented CB in the films with film thickness greater than 30 nm, and that the CB mesogens were oriented only planarly at 15 nm thickness.

http://dx.doi.org/10.5772/65090

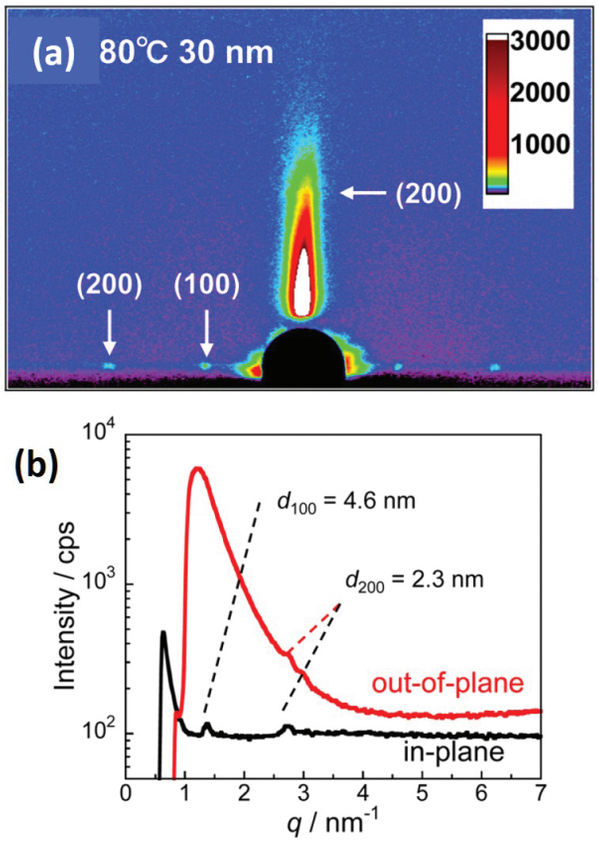

Figure 13. 2D GI-SAXS (Cu Kα) patterns (a) of PCBA films with a thickness of 30 nm at 80 °C. Lower figure (b) indicates 1D intensity profiles (black: in-plane; red: out-of-plane directions). Reprinted with permission from Tanaka et al. [71]. Copyright 2016 American Chemical Society.

GI-SAXS measurements with synchrotron tender X-rays (λ = 0.539 nm, 2.30 keV) were achieved at various α_i. **Figure 14** shows the 2D GI-SAXS images for 30 nm thick film at room temperature. The CB mesogens at this thickness as mentioned before are oriented both in the homeotropic and planar directions (coexistence). The α_c in this sample was estimated at about 0.54° for this X-ray energy. Under conditions of $\alpha_i < \alpha_c$ (α_c is about 0.54° for 2.30 keV), the scattering signals in the thin film was observed only the out-of-plane direction as shown in **Figure 14a** and **b**, where Λ is estimated as in the range less than 10–20 nm in these experimental conditions. It is apparently indicated that the CB mesogens adopt homeotropic orientation in the free surface region. When $\alpha_i > \alpha_c$, the out-of-plane scatterings were split into double peaks in the q_z direction as shown in **Figure 14c–e**. The split double peaks originate from the transmitted X-ray through the film and then reflected on the substrate [44]. Hence, the high q_z peak of the double peaks can be assigned to the scattering from the reflection path on the film surface. The split spots means that the X-ray beam actually travelled through the overall film thickness and reached the sample/substrate interface. When $\alpha_i > \alpha_c$ (Λ > 100 nm), the peaks appeared in-plane direction due to the planar orientation were clearly observed as shown in **Figure 14d–f** with arrows. These signals undoubtedly originate from the mesogens near the polymer/substrate interface.

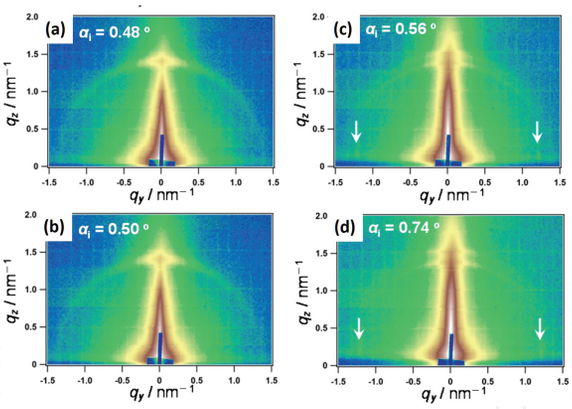

Figure 14. Two-dimensional GI-SAXS patterns for PCBA thin film with 30 nm thickness using tender X-rays (0.539 nm). Measurements were conducted at α_i = 0.48 (Λ = 11 nm) (a), 0.50 (Λ = 16 nm) (b), 0.56 (Λ = 167 nm) (c), 0.74 (Λ = 453 nm), and (d). Note that α_c (0.54°) is positioned between (b) and (c). Reprinted with permission from Tanaka et al. [71]. Copyright 2016 American Chemical Society.

From the overall data of UV-vis absorption spectroscopic [71] and the GISAXS measurements utilizing hard and tender X-rays, the orientation structural models of CB mesogens in PCBA thin films are schematically illustrated in **Figure 15**. In thick films with 140 nm, the CB mesogens are almost aligned homeotropically. However, a considerable number of the CB mesogens planarly anchored exist near the substrate (polymer/substrate interface) as revealed by GI-SAXS measurements with hard X-rays (**Figure 13**). At a thickness of 30 nm, the amounts of homeotropically and planarly oriented CB mesogens is comparable, where depth-resolved information is obtained by GI-SAXS with tender X-ray experiments (**Figure 14**). In the film thickness of 10–15 nm, the CB mesogens adopt almost planar alignment. When the film becomes further thinner from the critical level of 7 nm, the planar alignment near the surface disappears where the liquid crystal structuring (antiparallel packing of the CB mesogens) is lost.

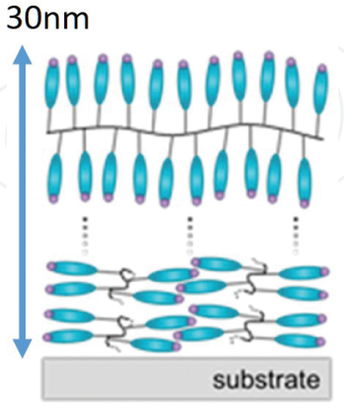

Figure 15. Schematic illustration of orientation of the CB mesogens in films with film thickness 30 nm. Purple circles indicate the cyano group at the terminal of mesogen. Note that the antiparallel interactions (LC structuring) are kept among the CB mesogens at thickness above 10–15 nm. Such LC structuring is lost at thickness of 7 nm. Reprinted with permission from Tanaka et al. [71]. Copyright 2016 American Chemical Society.

http://dx.doi.org/10.5772/65090

4. Grazing-incidence resonant soft X-ray scattering [50]

The GI-RSoXS is a novel technique, which is in particular suited for more complex system such as multicomponent block copolymer and polymer blend films. Resonant soft X-ray scattering has already been successful for probing morphology and spatial structure in organic photovoltaic (OPV) systems [85, 86] and triblock copolymer system [87]. GI-RSoXS allows for detecting near surface and inner structure separately at fixed incident angle by tuning X-ray photon energy because the penetration depth of the X-ray beam is drastically affected by the change in X-ray photon energy across the adsorption edge. Adsorption *K* edge for organic materials composed of mainly carbon, nitrogen, and oxygen are 284, 409, and 543 eV. The fine structure of the adsorption edge can be utilized in GISAXS measurements. Near edge X-ray adsorption fine structure (NEXAFS) spectrum needs to be probed for the polymeric materials in order to estimate the complex refractive index of X-ray that becomes important for depth-sensitive and component sensitive analyses. Typically, the NEXAFS spectra of polymers, which have low contrast in the real part of the refractive index in the hard photon energy regime, indicate considerable differences in the soft X-ray regime. In this section, investigation of nanostructure in the polymer blend thin film, poly(3-hexylthiophene) (P3HT) and poly[5-(2-ethylhexyloxy)-2-methoxycyanoterephtalylidene] (MEH-CN-PPV), is introduced as an example of GI-RSoXS experiment carried out by Ruderer et al. [50].

GI-RSoXS measurements with soft X-ray were conducted at the synchrotron beamline 11.0.1.2 of the advanced light source (ALS) at the LBNL in Berkeley (USA) [88, 89]. Due to the high adsorption of soft X-ray in air, full setup (sample and X-ray detector) was kept in high vacuum. The energy of X-ray was used in the range of 280–320 eV (λ: 4.4–3.9 nm). Sample-to-detector was 18.5 cm that was sufficient for detecting length scale in the range from 21 nm to a few micron meters. An incident angle $\alpha_i = 2°$, which is near the critical angle α_C of 2.3° for 280eV and 1.5° for 283 eV. The both polymers (P3HT and MEH-CN-PPV) were dissolved in chloroform. The thin film of polymer blend was prepared by spin coating from the solution; the thickness was controlled to be about 70 nm. The films were annealed at 200 °C for 10 min in air without degradation. The NEXAFS spectroscopy measurement was conducted for taking the wavelength dependent refractive index ($n = 1 - \delta + i\beta$) of polymers used here for electromagnetic radiation near the adsorption edge. NEAXFS spectra were also obtained at the same beam line of the ALS. The sample environment is identical to the GI-RSoXS setup. The polymer thin films were prepared on silicon nitride membranes and measured in transmission geometry. The adsorption part β of the refractive index was obtained through Beer's law. The real part δ of the refractive index was calculated from the β using Kramers-Krongis relation.

Figure 16a shows the X-ray energy dependence of the dispersion δ and the adsorption β of P3HT and MEH-CN-PPV homopolymer. The spectra of respective homo polymers are different. NEXAFS spectra of the blend system with different blend ratio can be obtained by a linear superposition of the spectra of P3HT and MEH-CN-PPV homopolymer weighted with the corresponding blend ratio. The dispersion δ spectra of P3HT and MEH-CN-PPV reveal positive and negative values and differ strongly depending X-ray energy. Therefore, the scattering contrast depends on the X-ray energy. Using the adsorption β spectra, the

penetration depth Λ of the soft X-rays into the blend film is calculated as shown in **Figure 16b**. **Figure 17** indicates the GI-RSoXS patterns of as spun P3HT/MEH-CN-PPV bulk heterojunction films with a P3HT content of 70 wt% for different energies from 280 to 289 eV (wavelength of X-rays from 4.43 to 4.29 nm). Although the wavelength is varied by only 3%, the scattering patterns significantly change. For energy below 284 eV, an intensity oscillation in vertical direction is observed, which comes from the correlated roughness originating from the interference of scattered X-rays from different interfaces. The correlated roughness vanishes with increasing energies of the X-rays. It indicates no scattering signal from the substrate interface is detected and X-ray penetrates near the surface as shown in **Figure 17**. The low scattering intensity of GI-RSoXS at 284 eV (**Figure 17c**) is due to the very low incident intensity at this energy. The reduction of the intensity at 286 eV (**Figure 17e**) can be ascribed to the significant low contrast between P3HT and MEH-CN-PPV at this energy. Thus, the surface structure is accessible at 286 eV. The change in the total scattered intensity was attributed to the changed contrast conditions from the contrast variation.

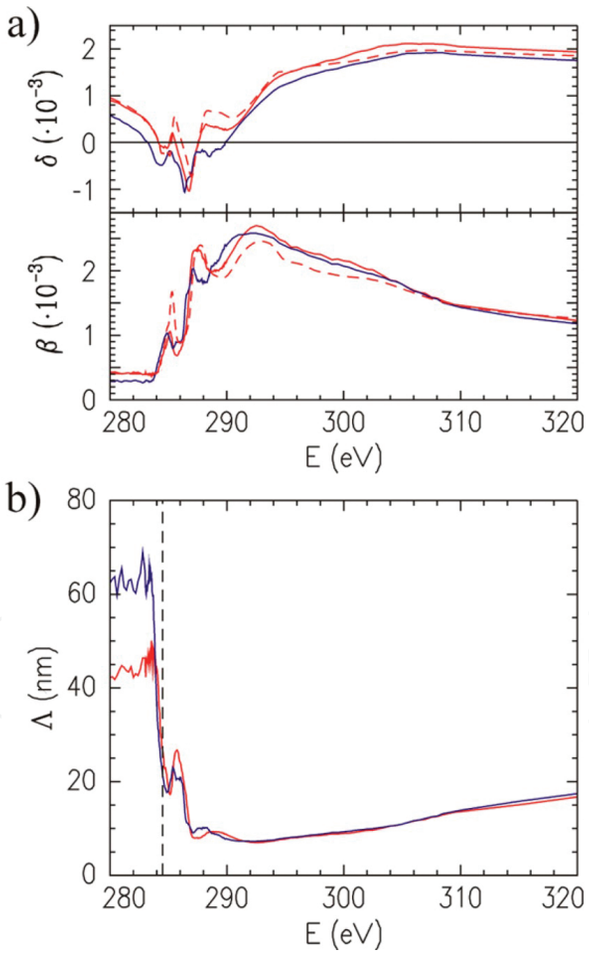

Figure 16. (a)Dispersion δ and the absorption β of P3HT (red solid lines) and MEH-CN-PPV (blue solid lines) as a function of the X-ray energy. For comparison, the calibrated P3HT spectra (dashed lines) from the database [90] are drawn. (b) Penetration depth of X-ray of P3HT (red) and MEH-CN-PPV (blue) as a function of X-ray energy. Reprinted with permission from Ruderer et al. [50]. Copyright 2016 American Chemical Society.

http://dx.doi.org/10.5772/65090

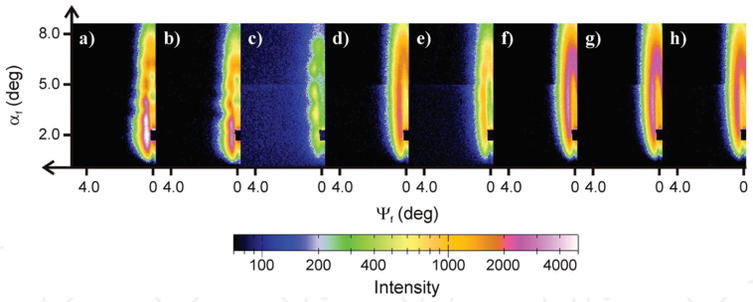

Figure 17. Two-dimensional GI-RSoXS patterns of as-spun P3HT: MEH-CN-PPV film with a P3HT content of 70 wt% with different X-ray energies. The X-ray energy: (a) 282, (b) 283, (c) 284, (d) 285, (e) 286, (f) 287, (g) 288, and (h) 289 eV. Copyright American Chemical Society, Ruderer et al. [50].

Author details

Katsuhiro Yamamoto

Address all correspondence to: yamamoto.katsuhiro@nitech.ac.jp

Department of Life Science and Applied Chemistry, Frontier Research Institute for Materials Science, Field of Soft Materials, Graduate School of Engineering, Nagoya Institute of Technology, Nagoya, Japan

References

[1] Zhang, Q.; Cirpan, A.; Russell, T. P.; Emrick, T. Donor-acceptor poly (thiophene-block-perylene diimide) copolymers: synthesis and solar cell fabrication. Macromolecules. 2009;42:1079–1082.

[2] Sun, S. S.; Zhang, C.; Ledbetter, A.; Choi, S.; Seo, K.; Bonner, C. E. Jr; Dress, M; Sariciftchi, N. S. Photovoltaic enhancement of organic solar cells by a bridged donor-acceptor block copolymer approach. Appl. Phys. Lett. 2007;90:043117.

[3] Crossland, E. J. W.; Kamperman, M.; Nedelcu, M.; Ducati, C.; Wiesner, U.; Smilges, D.-M.; Toombes, G. E. S.; Hilmyer, M. A.; Ludwigs, S.; Steiner, U.; Naith, H. J. A bicontinuous double gyroid hybrid solar cell. Nano Lett. 2008;9:2807–2812.

[4] Singh, G.; Yager, K.; Berry, B.; Kim, H.-C.; Karim, A. Dynamic thermal field-induced. ACS Nano. 2012;6:10335–10342.

[5] Luo, Y.; Montarnal, D.; Kim, S.; Shi, W.; Barteau, K. P.; Pester, C. W.; Hustad, P. D.; Christianson, M. D.; Fredrickson, G. H.; Kramer, E. J.; Hawker, C. J. Poly(dimethylsi-

loxane-b-methyl methacrylate): a promising candidate for sub-10 nm patterning. Macromolecules. 2015;48:3422–3430.

[6] Gu, W.; Zhao, H.; Wei, Q.; Coughlin, E. B.; Theato, P.; Russell, T. P. Line patterns from cylinder-forming photocleavable block copolymers. Adv. Mater. 2013;25:4690–4695.

[7] Wan, L.-S.; Li, J.-W.; Ke, B.-B.; Xu, Z.-K. Ordered microporous membranes template by breath figures for size-selective separation. J. Am. Chem. Soc. 2012;134:95098.

[8] Jeong, U.; Ryu, D. Y.; Kim, J. K.; Kim, D. H.; Wu, X.; Russell, T. P. Precise control of nanopore size in thin film using mixtures of asymmetric block copolymer and homopolymer. Macromoelcules. 2003;36:10126–10129.

[9] Matsen, M. W.; Schick, M. Stable and unstable phases of a diblock copolymer melt. Phys. Rev. Lett. 1994;72:2660–2663.

[10] Stein, G. E.; Kramer, E. J.; Li, X.; Wang, J. Layering transitions in thin films of spherical-domain block copolymers. Macromolecules. 2007;40:2453–2460.

[11] Suh, H. S.; Kang, H.; Nealey, P. F.; Char, K. Thickness dependence of neutral parameter windows for perpendicularly oriented block copolymer thin films. Macromolecules. 2010;43:4744–4751.

[12] Albert, J.; Epps, T. H. Self-assembly of block copolymer thin films. Mater. Today. 2010;13:24–44.

[13] Jung, J.; Park, H. W.; Lee, S.; Lee, H.; Chang, T.; Matsunaga, T.; Jinnai, H. Effect of film thickness on the phase behaviors of diblock copolymer thin film. ACS Nano. 2010;4:3109–3116.

[14] Luo, M.; Seppala, J. E.; Albert, J. N. L.; Lewis, R.; Mahadevapuram, N.; Stein, G. E.; Epps, T. H. Manipulating nanoscale morphologies in cylinder-forming poly (styrene-b-isoprene-b-styrene) thin films using film thickness and substrate surface chemistry gradient. Macromolecules. 2013;45:1803–1811.

[15] Kim, S. O.; Solak, H. H.; Stoykovich, M. P.; Ferrier, N. J.; Pablo, J. J.; Nealey, P. F. Epitaxial self-assembly of block copolymers on lithographically defined nanopatterned substrates. Nature. 2003;424:411–414.

[16] Shelton, C. K.; Epps, T. H. Decoupling substrate surface interactions in block polymer thin film self-assembly. Macromolecules. 2015;48:4572–4580.

[17] Mansky, P.; Liu, Y.; Huang, E.; Russell, T. P.; Hawker, C. Controlling polymer-surface interactions with random copolymer brushes. Science. 1997;275:1458–1460.

[18] Park, S.; Lee, D. H.; Xu, J.; Kim, B.; Hong, S. W.; Jeong, U.; Xu, T.; Russell, T. P.. Macroscopic 10-terabit–per–square-inch arrays from block copolymers with lateral order. Science. 2009;323:1030–1033.

[19] Sivaniah, E.; Hayashi, Y.; Iino, M.; Hashimoto, T.; Fukunaga, K. Observation of perpendicular orientation in symmetric diblock copolymer thin films on rough substrates. Macromolecules. 2003;36:5894–5896.

[20] Qiang, Z.; Zhang, L.; Stein, G. E.; Cavicchi, K. A.; Vogt, B. D. Macromolecules. Unidirectional Alignment of Block Copolymer Films Induced by Expansion of a Permeable Elastomer during Solvent Vapor Annealing. 2014;47:1109–1116.

[21] Xu, T.; Zvelindovsky, A. V.; Sevink, G. J. A.; Lyakhova, K. S.; Jinnai, H.; Russell, T. P. Electric field alignment of asymmetric diblock copolymer thin films. Macromolecules. 2005;38:10788–10798.

[22] Gopinadhan, M.; Majewski, P. W.; Osuji, C. O. Macromolecules. 2010;43:3286–3293.

[23] Fukuhara, K.; Nagano, S.; Hara, M.; Seki, T. Free-surface molecular command. Nat. Commun. 2014;5:3320.

[24] Sano, M.; Nakamura, S.; Hara, M.; Nagano, S.; Shinohara, Y.; Amemiya, Y.; Seki, T. Pathways toward photoinduced alignment switching in liquid crystalline block copolymer films. Macromolecules. 2014;47:7178–7186.

[25] Cui, G.; Ohya, S.; Matsutani, T.; Nagano, S.; Dohi, T.; Nakamura, S.; Sakurai, S.; Miyazaki, T.; Yamamoto, K. Perpendicular orientation of sub-10 nm channels in polystyrene-b-poly(4-hydroxyl styrene)/PEG oligomer blend thin films. Nanoscale. 2013;5:6713–6719.

[26] Gu, W.; Xu, J.; Kim, J.-K.; Hong, S. W.; Wei, X.; Yang, X.; Lee, K. Y.; Kuo, D. S.; Xiao, S.; Russell, T. P. Solvent-assisted directed self-assembly of spherical microdomain block copolymers to high areal density arrays. Adv. Mater. 2013;25:3677–3682.

[27] Kim, S. H.; Misner, M. J.; Yang, L.; Gang, O.; Ocko, B. M.; Russell, T. P. Salt complexation in block copolymer thin films. Macromolecules. 2013;39:8473–8479.

[28] Jeong, J. W.; Park, W. I.; Kim, M.-J.; Ross, C. A.; Jung, Y. S. Highly tunable self-assembled nanostructures from a poly(2-vinylpyridine-b-dimethylsiloxane) block copolymer. Nano Lett. 2011;11:4095–4101.

[29] Park, S.; Wang, J.-Y.; Kim, B.; Xu, J.; Russell, T. P. A simple route to highly oriented and ordered nanoporous block copolymer templates. ACS Nano. 2008;2:766–772.

[30] She, M.-S.; Lo, T.-Y.; Ho, R.-M. Long-range ordering of block copolymer cylinders driven by combining thermal annealing and substrate functionalization. ACS Nano. 2013;7:2000–2011.

[31] Tang, C.; Wu, W.; Smilgies, D. M.; Matyjaszewski, K.; Kowalewski, T. J. Am. Chem. Soc. Robust Control of Microdomain Orientation in Thin Films of Block Copolymers by Zone Casting. 2011;133:11802–11809.

[32] De Rosa, C.; Park, C.; Thomas, E. L.; Lotz, B. Nature. Microdomain patterns from directional eutectic solidification and epitaxy. 2000;405:433–437.

[33] Reiter, G.; Castelein, G.; Hoerner, P.; Riess, G.; Blumen, A.; Sommer, J. U. Phys. Rev. Lett. Nanometer-Scale Surface Patterns with Long-Range Order Created by Crystallization of Diblock Copolymers. 1999;83:3844–3847.

[34] Niihara, K.; Matsuwaki, U.; Torikai, N.; Atarashi, H.; Tanaka, K.; Jinnai, H. Macromolecules. A Novel Structural Analysis for a Cylinder-Forming Block Copolymer Thin Film Using Neutron Reflectivity Aided by Transmission Electron Microtomography. 2007;40:6940–6946.

[35] Yokoyama, H.; Kramer, E. J.; Rafailovich, M. H.; Sokolov, J.; Schwarz, S. A. Macromolecules. Structure and Diffusion of Asymmetric Diblock Copolymers in Thin Films: A Dynamic Secondary Ion Mass Spectrometry Study. 1998;31:8826–8830.

[36] Ninomiya, S.; Ichiki, K.; Yamada, H.; Nakata, Y.; Seki, T.; Aoki, T.; Matsuo, J. Rapid Commun. Mass Spectrom. 2009;23:1601.

[37] Terlier, T.; Tiron, R.; Gharbi, A.; Chevalier, X.; Veillerot, M.; Martinez, E.; Barnes, J. P. Surf. Interface Anal. 2014;46:83–91.

[38] Gilbert, J. B.; Rubner, M. F.; Cohen, R. E. Proc. Natl. Acad. Sci. U. S. A. 2013;110:6651–6656.

[39] Gilbert, J. B.; Luo, M.; Shelton, C. K.; Rubner, M. F.; Cohen, R. E.; Epps, T. H. III . ACS Nano. 2015;9:512–520.

[40] Mayes, A. M.; Russell, T. P.; Bassereau, P.; Baker, S. M.; Smith G. S. Macromolecules. 1994;27:749–755.

[41] Koneripalli, N.; Singh, N.; Levicky, R.; Bates, F. S.; Gallagher, P. D.; Satija, K. Macromolecules. 1995;28:2897–2904.

[42] Müller-Buschbaum, P. Anal. Bioanal. Chem. 2003;376:3–10.

[43] Roth, S. V.; Burghammer, M.; Riekel, C.; Bushbaum, P. M. Appl. Phys. Lett. 2003;82:1935–1937.

[44] Lee, B.; Park, I.; Yoon, J.; Park, S.; Kim, J.; Kim, K. W.; Chang, T.; Ree, M.. Macromolecules. 2005;38:4311–4323.

[45] Yoon, J.; Yang, S. Y.; Lee, B.; Joo, W.; Heo, K.; Kim, J. K.; Ree, M. J. Appl. Crystallogr. 2007;40:305–312.

[46] Busch, P.; Smilgies, D. M.; Rauscher, M.; Posselt, D.; Papadakis, C. M. J. Appl. Crystallogr. 2006;39:433–442.

[47] Busch, P.; Posselt, D.; Smilgies, D. M.; Rauscher, M.; Papadakis, C. M. Macromolecules. 2007;40:630–640.

[48] Okuda, H.; Takeshita, K.; Ochiai, S.; Sakurai, S.; Kitajima, Y. J. Appl. Crystallogr. 2011;44:380–384.

[49] Wernecke, J.; Okuda, H.; Ogawa, H.; Siewert, F.; Krumrey, M. Macromolecules. 2014;47:5719–5727.

[50] Ruderer, M. A.; Wang, C.; Schaible, E.; Hexemer, A.; Xu, T.; Müller-Buschbaum, P. Macromolecules. 2013;46:4491–4501.

[51] Müler-Buschbaum, P.; Maurer, E.; Bauer, E.; Cubitt, R. Langmuir. 2006;22:9295–9303.

[52] Müller-Buschbaum, P.; Schulz, L.; Metwalli, E.; Moulin, J.-F.; Cubitt, R. Langmuir. 2009;25:4235–4242.

[53] Busch, P.; Rauscher, M.; Moulin, J.-F.; Müller-Buschbaum, P. J. Appl. Crystallogr. 2011;44:370–379.

[54] Müller-Buschbaum, P.; Schulz, L.; Metwalli, E.; Moulin, J.-F.; Cubitt, R. Langmuir. 2008;24:7638–7644.

[55] Müller-Buschbaum, P.; Kaune, G.; Haese-Seiller, M.; Moulin, J.-F. J. Appl. Crystallogr. 2014;47:1228–1237.

[56] Müller-Buschbaum P. Grazing incidence small-angle neutron scattering: challenges and possibilities. Polymer J. 2013;45:34–42. DOI: 0.1038/pj.2012.190

[57] Saito, I.; Miyazaki, T.; Yamamoto, K. Depth-resolved structure analysis of cylindrical microdomain in block copolymer thin film by grazing-incidence small-angle X-ray scattering utilizing low-energy X-rays. Macromolecules. 2015;48:8190−8196. DOI: 10.1021/acs.macromol.5b01883

[58] Yin, J.; Yao, X.; Liou, J.-Y.; Sun, W.; Sun, Y.-S.; Wang, Y. ACS Nano. 2013;7:9961–9974.

[59] Kim, J.; Lew, B.; Kim, W. S. Nanoscale Res. Lett. 2011;6:616.

[60] Photon-Factory KEK. BL-15A2: High-brilliance Small-Angle X-ray Scattering beamline [Internet]. Available from: http://pfwww.kek.jp/saxs/beamline/bl15a2.html

[61] Sinha, S. K.; Sirota, E. B.; Garoff, S. Phys. Rev. B: Condens. Matter. Mater. Phys. X-ray and neutron scattering from rough surfaces. 1988;38:2297–2311.

[62] Yamamoto, T.; Okuda, H.; Takeshita, K.; Usami, N.; Kitajima, Y.; Ogawa, H. J. Synchrotron Radiat. Grazing-incidence small-angle X-ray scattering from Ge nanodots self-organized on Si(001) examined with soft X-rays. 2014;21:161−164.

[63] Tokarev, I.; Krenek, R.; Burkov, Y.; Schmeisser, D.; Sidorenko, A.; Minko, S.; Stamm, M. Macromolecules. Microphase Separation in Thin Films of Poly(styrene-block-4-vinylpyridine) Copolymer−2-(4′-Hydroxybenzeneazo)benzoic Acid Assembly. 2005;38:507−516.

[64] Saito, I.; Shimada, D.; Aikawa, M.; Miyazaki, T.; Shimokita, K.; Takagi, H.; Yamamoto, K. Orientation and relaxation behaviors of lamellar microdomains of poly(methyl methacrylate)-b-poly(n-butyl acrylate) thin films as revealed by grazing-incidence small-angle X-ray scattering. Polymer J. 2016;48:399–406. DOI: 10.1038/pj.2016.2

[65] Ogawa, H.; Masunaga, H.; Sasaki, S.; Goto, S.; Tanaka, T.; Seike, T.; Takahashi, S.; Takeshita, K.; Nariyama, N.; Ohashi, H.; Ohata, T.; Furukawa, Y.; Matsushita, T.; Ishizawa, Y.; Yagi, N.; Takata, M.; Kitamura, H.; Takahara, A.; Sakurai, K.; Tashiro, K.; Kanaya, T.; Amemiya, Y.; Horie, K.; Takenaka, M.; Jinnai, H.; Okuda, H.; Akiba, I.; Takahashi, I.; Yamamoto, K.; Hikosaka, M.; Sakurai, S.; Shinohara, Y.; Sugihara, Y.; Okada, A. Experimental station for multiscale surface structural analyses of oft-material films at SPring-8 via a GISWAX/GIXD/XR-integrated system. Polymer J. 2012;45:109–116.

[66] Masunaga, H.; Ogawa, H.; Takano, T.; Sasaki, S.; Goto, S.; Tanaka, T.; Seike, T.; Takahashi, S.; Takeshita, K.; Nariyama, N.; Ohashi, H.; Ohata, T.; Furukawa, Y.; Matsushita, T.; Ishizawa, Y.; Yagi, N.; Takata, M.; Kitamura, H.; Sakurai, K.; Tashiro, K.; Takahara, A.; Amamiya, Y.; Horie, K.; Takenaka, M.; Kanaya, T.; Jinnai, H.; Okuda, H.; Akiba, I.; Takahashi, I.; Yamamoto, K.; Hikosaka, M.; Sakurai, S.; Shinohara, Y.; Okada, A.; Sugihara, Y. Multipurpose soft-material SAXS/WAXS/GISAXS beamline at SPring-8. Polymer J. 2011;43:471–477.

[67] Russell, T. P.; Coulon, G.; Deline, V. R.; Miller, D. C. Characteristics of the surface-induced orientation for symmetric diblock PS/PMMA copolymers. Macromolecules. 1989;22:4600–4604.

[68] Kawaguchi, D.; Tanaka, K.; Kajiyama, T.; Takahara, A.; Tasaki, S. Mobility gradient in surface region of monodisperse polystyrene films. Macromolecules. 2003;36:1235–1240.

[69] Kajiyama, T.; Tanaka, K.; Takahara, A. Depth dependence of the surface glass transition temperature of a poly (styrene-block-methyl methacrylate) diblock copolymer film on the basis of temperature-dependent x-ray photoelectron spectroscopy. Macromolecules. 1995;28:3482–3484.

[70] Inoue, R.; Kawashima, K.; Matsui, K.; Nakamura, M. Interfacial properties of polystyrene thin films as revealed by neutron reflectivity. Phys. Rev. E. 2011;84:031802.

[71] Tanaka, D.; Mizuno, T.; Hara, M.; Nagano, S.; Saito, I.; Yamamoto, K.; Seki, T. Evaluations of mesogen orientation in thin films of polyacrylate with cyanobiphenyl side chain. Langmuir. 2016;32:3737–3745. DOI: 10.1021/acs.langmuir.6b00538

[72] Henn, G.; Stamm, M.; Poths, H.; Rücker, M.; Rabe, J. P. Influence of order in thin smectic polymer films on the structure at the surface. Phys. B. 1966;221:174–184.

[73] Mensinger, H.; Stamm, M.; Boeffel, C. Order in thin films of a liquid crystalline polymer. J. Chem. Phys. 1992;96:3183–3190.

[74] Elben, H.; Strobl, G.. Smectic surface structures in the isotropic phase of liquid-crystalline polymers studied by x-ray reflectivity. Macromolecules. 1993;26:1013–1018.

[75] van der Wielen, M. W. J.; Cohen Stuart, M. A.; Fleer, G. J.; de Boer, D. K. G.; Leenaers, A. J. G.; Nieuwhof, R. P.; Marcelis, A. T. M.; Sudhölter, E. J. R. Order in thin films of side-chain liquid-crystalline polymers. Langmuir. 1997;13:4762−4766.

[76] van der Wielen, M. W. J.; Cohen Stuart, M. A.; Fleer, G. J. Autophobicity and layering behavior of thin liquid-crystalline polymer films. Langmuir. 1998;14:7065–7071.

[77] Wu, J.-S.; Fasolka, M. J.; Hammond, P. T. Mixed surface morphologies of well-defined smectic diblock copolymer ultrathin films. Macromolecules. 2000;33. DOI: 1108-1110

[78] Morikawa, Y.; Nagano, S.; Watanabe, K.; Kamata, K.; Iyoda, T.; Seki, T. Optical alignment and patterning of nanoscale microdomains in a block copolymer thin film. Adv. Mater. 2006;18:883−886.

[79] Uekusa, T.; Nagano, S.; Seki, T. Highly ordered in-plane photoalignment attained by the brush architecture of liquid crystalline azobenzene polymer. Macromolecules. 2009;42:312–318.

[80] Haque, H. A.; Kakehi, S.; Hara, M.; Nagano, S.; Seki, T. High density liquid-crystalline azobenzene polymer brush attained by surface-initiated ring-opening metathesis polymerization. Langmuir. 2013;29:7571–7575.

[81] Asaoka, S.; Uekusa, T.; Tokimori, H.; Komura, M.; Iyoda, T.; Yamada, T.; Yoshida, H. Normally oriented cylindrical nanostructures in amphiphilic PEO–LC diblock copolymers films. Macromolecules. 2011;44:7645−7658.

[82] Fukuhara, K.; Fujii, Y.; Nagashima, Y.; Hara, M.; Nagano, S.; Seki, T. Liquid-crystalline polymer and block copolymer domain alignment controlled by free-surface segregation. Angew. Chem. Int. Ed. 2013;52:5988–5991.

[83] Komura, M.; Yoshitake, A.; Komiyama, H.; Iyoda, T. Control of air-interface-induced perpendicular nanocylinder orientation in liquid crystal block copolymer films by a surface-covering method. Macromolecules. 2015;48:672−678.

[84] Tanaka, D.; Nagashima, Y.; Hara, M.; Nagano, S.; Seki, T. Alternation of side-chain mesogen orientation caused by the backbone structure in liquid-crystalline polymer thin films. Langmuir. 2015;31:11379–11383.

[85] Swaraj, S.; Wang, C.; Yan, H.; Watts, B.; Lüning, J.; McNeill, C. R.; Ade, H. Nano Lett. Nanomorphology of Bulk Heterojunction Photovoltaic Thin Films Probed with Resonant Soft X-ray Scattering. 2010;10:2863–2869.

[86] Chen, W.; Xu, T.; He, F.; Wang, W.; Wang, C.; Strzalka, J.; Liu, Y.; Wen, J.; Miller, D. J.; Chen, J.; Hong, K.; Yu, L.; Darling, S. B. Nano Lett. Hierarchical Nanomorphologies Promote Exciton Dissociation in Polymer/Fullerene Bulk Heterojunction Solar Cells. 2011;11:3707–3713.

[87] Wang, C.; Lee, D. H.; Hexamer, A.; Kim, M. I.; Zhao, W.; Hasegawa, H.; Ade, H.; Russell, T. P. Nano Lett. Defining the Nanostructured Morphology of Triblock Copolymers Using Resonant Soft X-ray Scattering. 2011;11:3906–3911.

[88] Wang, C.; Hexemer, A.; Nasiatka, J.; Chan, E. R.; Young, A. T.; Padmore, H. A.; Schlotter, W. F.; Lüning, J.; Swaraj, S.; Watts, B.; Gann, E.; Yan, H.; Ade, H. IOP Conf. Ser.: Mater. Sci. Eng. Resonant Soft X-ray Scattering of Polymers with a 2D Detector: Initial Results and System Developments at the Advanced Light Source. 2010;14:012016.

[89] Gann, E.; Young, A. T.; Collins, B. A.; Yan, H.; Nasiatka, J.; Padmore, H. A.; Ade, H.; Hexemer, A.; Wang, C. Rev. Sci. Instrum. Soft x-ray scattering facility at the Advanced Light Source with real-time data processing and analysis. 2012;83:045110.

[90] Watts, B.; Swaraj, S.; Nordlund, D.; Lüning, J.; Ade, H. J. Chem. Phys. Calibrated NEXAFS spectra of common conjugated polymers. 2011;134:024702.